

UNIVERSIDAD DE CONCEPCIÓN



CENTRO DE INVESTIGACIÓN EN
INGENIERÍA MATEMÁTICA (CI²MA)



A new mathematical model for verifying the Navier-Stokes
compatibility of 4D flow MRI data

CRISTÓBAL BERTOGLIO, CRISTIAN CÁRCAMO,
JEREMÍAS GARAY, HERNÁN MELLA,
JOAQUÍN MURA, JULIO SOTELO,
SERGIO URIBE

PREPRINT 2021-01

SERIE DE PRE-PUBLICACIONES

A new mathematical model for verifying the Navier-Stokes compatibility of 4D flow MRI data

Jeremías Garay, Hernán Mella, Julio Sotelo, Cristian Cárcamo,
Sergio Uribe, Cristóbal Bertoglio^{*†}, Joaquín Mura

Abstract

A new model to determine the quality of three-dimensional, time-resolved MRI velocity measurements is presented. By assuming that the true flow velocity satisfies the incompressible Navier-Stokes equations, it is decomposed by measurements \mathbf{u}_{meas} plus a corrective field \mathbf{w} . Therefore, a non-linear problem for the corrective field. We first introduce the continuous formulation, developing and analyzing a stabilized finite element formulation tailored to this problem. Then, extensive numerical examples – using synthetic and experimental data – illustrate the potential to use \mathbf{w} for assessing the quality of the measurements under the main sources of error encountered in practice: noise and aliasing.

1 Introduction

Time-resolved 3D flow magnetic resonance imaging, also referred as 4D flow MRI, has shown in the last years increasing potential in the assessment of cardiovascular diseases since it offers a full coverage of the region of interest [1, 2]. This makes possible the computation of several hemodynamic parameters which can be used as new biomarkers [2]. However, high-quality 4D flow in subjects involves long time scans (>20 minutes) even with coarse spatio-temporal resolutions making it challenging for everyday clinical use. In order to accelerate the acquisition time, several strategies have been proposed such as parallel imaging [3, 4], which accelerates the acquisition by exploiting the sensitivity of multiple receivers, and k-space undersampling [5, 6, 7, 8], which exploits data redundancies in frequency and time. This scan time reduction comes at the price of reducing the signal-to-noise ratio (SNR) and the appearance of imaging artifacts. Moreover, the velocity field can only be obtained under certain predefined velocity ranges, which depend of the setup of the magnetic gradients,

^{*}Both C. Bertoglio and J. Mura are joint last authors, listed in alphabetical order.

[†]Corresponding author: c.a.bertogliorug.nl

therefore being often subject of velocity aliasing. Further artifacts may also appear due to subject’s respiration and motion during the scan.

To the best of the authors knowledge, quality control of 4D flow is based on direct calculation and inspection of the velocity data, such as peak/mean flows, mean velocities, flow patterns and stroke volumes [9, 10, 2]. A more systematic approach is to compute the divergence field of the data: assuming the blood flow is incompressible, jumps in the divergence field may indicate the presence of artifacts. Indeed, the incompressibility assumption has been used for denoising [11, 12, 9, 13] and as a regularization during the reconstruction process [14, 15]. However, limitations of the divergence are that it does not allow to analyze between each velocity component separately, and it cannot be compared against the “true” value: every non-zero value is infinitely large compared with zero. Moreover, there exist relevant perturbed configurations which lead to zero-divergence fields too, as the Womersley flow in a tube with velocity aliasing in the longitudinal spatial direction.

Therefore, this work introduces an alternative quantitative approach for assessing 4D flow quality by verifying the compatibility with respect to the linear momentum conservation part of the Navier-Stokes, which written appropriately, includes also angular momentum and mass conservation too.

The rest of this article is structured as follows. In Section 2, the mathematical model will be introduced, and a numerical method will be developed and analyzed. In Section 3, a set of relevant examples, using synthetic data, will be detailed. Numerical computations of the new model for several types of artifacts and its comparison against the divergence of the data is also shown. Real 4D flow MRI data results are shown in Section 4. Finally, in Section 5 we discuss potential applications of this metric in the context of reconstruction and processing 4D flow MRI.

2 The mathematical model

2.1 The continuous problem

We assume a physical velocity, denoted by \mathbf{u} , which satisfies the Navier-Stokes equations in the vessel lumen Ω :

$$\rho \frac{\partial \mathbf{u}}{\partial t} + \rho(\mathbf{u} \cdot \nabla)\mathbf{u} - \mu \Delta \mathbf{u} + \nabla p = 0 \quad \text{in } \Omega \quad (1)$$

with ρ and μ the density and dynamic viscosity of the fluid, respectively. Note that, although this being the conservation of linear momentum, the used form considers additionally the conservation of angular momentum together with mass conservation.

Let us denote \mathbf{u}_{meas} the 4D Flow measurement. We assume that there exist a corrector field \mathbf{w} , that satisfies:

$$\mathbf{u} = \mathbf{u}_{meas} + \mathbf{w} \quad \text{in } \Omega \quad (2)$$

$$\nabla \cdot \mathbf{w} = 0 \quad \text{in } \Omega \quad (3)$$

$$\mathbf{w} = \mathbf{0} \quad \text{on } \partial\Omega \quad (4)$$

By writing (1) in weak form, and using relations (2)-(4), we can formulate the following weak problem: Find $(\mathbf{w}(t), p(t)) \in H_0^1(\Omega) \times L_0^2(\Omega)$ such that

$$\begin{aligned} \int_{\Omega} \rho \frac{\partial \mathbf{w}}{\partial t} \cdot \mathbf{v} + \rho((\mathbf{u}_{meas} + \mathbf{w}) \cdot \nabla) \mathbf{w} \cdot \mathbf{v} + \rho(\mathbf{w} \cdot \nabla) \mathbf{u}_{meas} \cdot \mathbf{v} + \mu \nabla \mathbf{w} : \nabla \mathbf{v} - p \nabla \cdot \mathbf{v} + q \nabla \cdot \mathbf{w} \\ = - \int_{\Omega} \rho \frac{\partial \mathbf{u}_{meas}}{\partial t} \cdot \mathbf{v} + \rho(\mathbf{u}_{meas} \cdot \nabla) \mathbf{u}_{meas} \cdot \mathbf{v} + \mu \nabla \mathbf{u}_{meas} : \nabla \mathbf{v} \end{aligned} \quad (5)$$

for all $(\mathbf{v}, q) \in H_0^1(\Omega) \times L_0^2(\Omega)$.

The following remarks are in order.

Remark 1 *The left-hand-side of Problem (5) resembles the one of the incompressible Navier-Stokes equation, up to two additional terms. Unfortunately, none of these terms are positive (this will become clear in the analysis in the next section), hence making the analysis of the well posedness of this continuous problem (existence, uniqueness, time-stability) an important mathematical challenge. However, at the discrete level those properties can be ensured by including adequate stabilization terms and constraints on the physical constants.*

Remark 2 *Equation (1) uses the so-called convective form of the advective term. While alternative forms of Equation (5) could be derived starting from other forms for the advection (e.g. conservative), the resulting discrete problem will need to be stabilized to obtain a solvable problem, leading to the same expression for the bilinear form. There will be indeed a difference on right-hand-side terms. There is, however, no particular reason to choose one above the other since all formulations are consistent with perfect (i.e. divergence-free) measurements.*

Remark 3 *An alternative formulation for the corrector field could be formulated by defining:*

$$\nabla \cdot \mathbf{w} = -\nabla \cdot \mathbf{u}_{meas} + \frac{1}{|\Omega|} \int_{\partial\Omega} \mathbf{u}_{meas} \cdot \mathbf{n} \quad (6)$$

instead of (3), where the second term in the right-hand-side is needed in order to enforce the compatibility with respect to the boundary condition (4). However, as it is shown in Appendix 5, this leads \mathbf{w} to have spurious larger values than using the divergence-free model even with perfect synthetic data and comparable in magnitude with the true velocity itself for realistic flows.

Remark 4 *Note that the so-called “STE” method for pressure reconstruction [16] corresponds to this method but dropping the first four terms of the right-hand-side.*

2.2 Stabilized finite element formulation

In order to aim to the clinical applicability of such data quality measure, it is crucial to use numerical schemes that are fast to compute and robust.

We assume first that a structured medical image is segmented and a mesh of the vessel domain created with constant element size h , using e.g. the tetrahedral mesh generator

reported in [17]. Denote the domain defined by that mesh Ω_h , which will allow to define the function spaces

$$V_h = \{\mathbf{w} \in [H_0^1(\Omega_h)]^3 : \mathbf{w} \in [\mathbb{P}_1(K)]^3 \forall K \in \Omega_h\}$$

and

$$Q_h = \{q \in L_0^2(\Omega_h) \cap H^1(\Omega_h) : q \in \mathbb{P}_1(K) \forall K \in \Omega_h\}$$

For the spatial discretization, we then adopt V_h and Q_h as solution spaces for \mathbf{w} and p , respectively, requiring to introduce additional stabilization terms for the convection and the pressure to ensure solvability.

For the time discretization, we adopt a backward Euler method with fixed time step τ to avoid GCL-type conditions on the meshes. In order to avoid a rootfinding problem at each time step (which can be hard to make it converge for large time steps and large right hand sides) the non-linear term on \mathbf{w} will be treated semi-implicitly.

The resulting fully discrete stabilized formulation reads as follows. Given $\mathbf{w}^0 = \mathbf{0}$, find $(\mathbf{w}^k, p^k) \in V_h \times Q_h$ such that

$$\mathcal{B}_k(\mathbf{w}^k, p^k; \mathbf{v}, q) = \mathcal{L}_j(\mathbf{v}, q) \quad (7)$$

for all $(\mathbf{v}, q) \in V_h \times Q_h$. The bilinear form is defined as:

$$\mathcal{B}_k(\mathbf{w}, p; \mathbf{v}, q) := A_k(\mathbf{w}, p; \mathbf{v}, q) + S_k^{conv}(\mathbf{w}; \mathbf{v}) + S_k^{press}(\mathbf{w}, p; \mathbf{v}, q) \quad (8)$$

with

$$A_k(\mathbf{w}, p; \mathbf{v}, q) := \int_{\Omega} \frac{\rho}{\tau} \mathbf{w} \cdot \mathbf{v} + \rho((\mathbf{u}_{meas}^k + \mathbf{w}^{k-1}) \cdot \nabla) \mathbf{w} \cdot \mathbf{v} + \rho(\mathbf{w} \cdot \nabla) \mathbf{u}_{meas}^k \cdot \mathbf{v} + \mu \nabla \mathbf{w} : \nabla \mathbf{v} - p \nabla \cdot \mathbf{v} + q \nabla \cdot \mathbf{w}$$

the bilinear form associated to the non-stabilized weak form of (5), while the convection stabilization term is given by

$$S_k^{conv}(\mathbf{w}; \mathbf{v}) := \int_{\Omega} \frac{\rho}{2} (\nabla \cdot (\mathbf{u}_{meas}^k + \mathbf{w}^{k-1})) \mathbf{w} \cdot \mathbf{v}$$

and the pressure stabilization term as

$$S_k^{press}(\mathbf{w}, p; \mathbf{v}, q) := \frac{\delta h^2}{\mu} \int_{\Omega_h} \left(\rho((\mathbf{u}_{meas}^k + \mathbf{w}^{k-1}) \cdot \nabla) \mathbf{w} + \rho(\mathbf{w} \cdot \nabla) \mathbf{u}_{meas}^k + \nabla p \right) \cdot \left(\rho((\mathbf{u}_{meas}^k + \mathbf{w}^{k-1}) \cdot \nabla) \mathbf{v} + \rho(\mathbf{v} \cdot \nabla) \mathbf{u}_{meas}^k + \nabla q \right) \quad (9)$$

with $\mathbf{f}^k = -\rho(\mathbf{u}_{meas}^k - \mathbf{u}_{meas}^{k-1})/\tau - \rho(\mathbf{u}_{meas}^k \cdot \nabla) \mathbf{u}_{meas}^k$ and $\delta > 0$ some user-defined parameter. Finally, the right-hand-side is given by

$$\mathcal{L}_j(\mathbf{v}, q) := \int_{\Omega} \frac{\rho}{\tau} \mathbf{w}^{k-1} \cdot \mathbf{v} + \ell_j(\mathbf{v}, q) \quad (10)$$

with

$$\begin{aligned} \ell_j(\mathbf{v}, q) &:= \int_{\Omega} \mathbf{f}^k \cdot \mathbf{v} - \mu \nabla \mathbf{u}_{meas}^k : \nabla \mathbf{v} \\ &\quad + \frac{\delta h^2}{\mu} \int_{\Omega_h} \mathbf{f}^k \cdot \left(\rho ((\mathbf{u}_{meas}^k + \mathbf{w}^{k-1}) \cdot \nabla) \mathbf{v} + \rho (\mathbf{v} \cdot \nabla) \mathbf{u}_{meas}^k + \nabla q \right) \end{aligned} \quad (11)$$

Remark 5 The stabilization term S_k^{conv} is in general not consistent with the solution of (5). However, it is indeed consistent when the measurements are perfect since in such case $\mathbf{w} = \mathbf{0}$ and $\nabla \cdot \mathbf{u}_{meas} = 0$. The stabilization term S_k^{press} is weakly consistent due to the inclusion of h^2 .

2.3 Existence and uniqueness of the discrete solution

The purpose is now to determine if Problem (7) is well-posed by verifying if the Lax-Milgram theorem is satisfied.

First, note that $\mathbf{u}_{meas}^k \in [H^1(\Omega_h)]^3$ for all k since the velocity values lie within a bounded finite interval, and then they are interpolated to \mathbb{P}_1 finite elements.

Denote the space of the whole solution vector $W = V_h \times Q_h$, then we can prove the following results.

Lemma 1 The operator $\|\cdot\|_W : W \rightarrow \mathbb{R}$ defined by

$$\|(\mathbf{v}, q)\|_W^2 := \beta \|\mathbf{v}\|_{H^1(\Omega_h)}^2 + S_k^{press}(\mathbf{v}, q; \mathbf{v}, q)$$

is a norm on $W = V_h \times Q_h$ for $\beta > 0$.

Proof The first term defines a norm in V_h and the second term is a seminorm in W , so $\|\cdot\|_W$ is a seminorm in W . It remains to proof that $\|(\mathbf{v}, q)\|_W = 0 \Rightarrow (\mathbf{v}, q) = \mathbf{0}$. Indeed, the first two terms have to be zero and therefore $\mathbf{v} = \mathbf{0}$. Therefore, ∇q has to be a constant and also zero-valued since $q \in Q_h$. ■

Lemma 2 For $\mathbf{v}, \mathbf{w} \in \mathbb{R}^d, \mathbf{C} \in \mathbb{R}^{d \times s}$ the following relation holds:

$$\mathbf{w} \cdot \mathbf{C} \mathbf{v} \leq \|\mathbf{C}\|_{\infty} \|\mathbf{w}\|_1 \|\mathbf{v}\|_1 \leq d \|\mathbf{C}\|_{\infty} \|\mathbf{w}\|_2 \|\mathbf{v}\|_2$$

with $\|\cdot\|_j$ denoting the ℓ^j -norm in \mathbb{R}^d .

Proof Directly from the lemma's definition. ■

Lemma 3 There exists $\alpha > 0$ such that:

$$\mathcal{B}_k(\mathbf{w}, p; \mathbf{w}, p) > \|(\mathbf{w}, p)\|_W^2 \quad (12)$$

$\forall (\mathbf{w}, p) \in W \setminus \{\mathbf{0}\}$ under the condition:

$$\rho/\tau + C_{\Omega}^{-2} \mu/2 - \rho 3 \|\nabla \mathbf{u}_{meas}^k\|_{\infty} > 0 \quad (13)$$

Proof Using standard arguments, Poincaré's inequality and Lemma 2 the following relation holds:

$$\begin{aligned}
A_k(\mathbf{w}, p; \mathbf{w}, p) + S_k^{conv}(\mathbf{w}; \mathbf{w}) &= \int_{\Omega} \frac{\rho}{\tau} \|\mathbf{w}\|_2^2 + \mu \|\nabla \mathbf{w}\|_2^2 + \rho (\mathbf{w} \cdot \nabla) \mathbf{u}_{meas}^k \cdot \mathbf{w} \\
&\geq \left(\frac{\rho}{\tau} + \frac{\mu}{2C_{\Omega}^2} \right) \|\mathbf{w}\|_{L_2(\Omega_h)}^2 + \rho \int_{\Omega} (\mathbf{w} \cdot \nabla) \mathbf{u}_{meas}^k \cdot \mathbf{w} + \frac{\mu}{2} \|\nabla \mathbf{w}\|_{L_2(\Omega_h)}^2 \\
&\geq \left(\frac{\rho}{\tau} + \frac{\mu}{2C_{\Omega}^2} - \rho 3 \|\nabla \mathbf{u}_{meas}^k\|_{\infty} \right) \|\mathbf{w}\|_{L_2(\Omega_h)}^2 + \frac{\mu}{2} \|\nabla \mathbf{w}\|_{L_2(\Omega_h)}^2 \\
&\geq \beta \|\mathbf{w}\|_{H_1(\Omega_h)}^2
\end{aligned}$$

with

$$\beta = \min(\rho/\tau + C_{\Omega}^{-2} \mu/2 - \rho 3 \|\nabla \mathbf{u}_{meas}^k\|_{\infty}, \frac{\mu}{2}) > 0$$

under condition (13). By adding the remaining term $S_k^{press}(\mathbf{w}, p; \mathbf{w}, p)$, relation (12) follows directly from the definition of the norm. ■

Lemma 4 *There exists a constant $M > 0$ such that:*

$$|\mathcal{B}_k(\mathbf{w}, p; \mathbf{v}, q)| \leq M \|(\mathbf{w}, p)\|_W \|(\mathbf{v}, q)\|_W$$

for all $(\mathbf{w}, p), (\mathbf{v}, q) \in W$.

Proof Since

$$|\mathcal{B}_k(\mathbf{w}, p; \mathbf{v}, q)| \leq |A_k(\mathbf{w}, p; \mathbf{v}, q)| + |S_k^{conv}(\mathbf{w}; \mathbf{v})| + |S_k^{press}(\mathbf{w}, p; \mathbf{v}, q)|$$

Using Cauchy-Schwarz inequality and adding the missing norm terms in \mathbf{w} we obtain

$$|S_k^{press}(\mathbf{w}, p; \mathbf{v}, q)| \leq \|(\mathbf{w}, p)\|_W \|(\mathbf{v}, q)\|_W$$

For the other terms, we can integrate the convective term by parts (hence canceling out the convective stabilization) and the pressure and divergence terms. Proceeding then using Cauchy-Schwarz:

$$\begin{aligned}
|A_k(\mathbf{w}, p; \mathbf{v}, q) + S_k^{conv}(\mathbf{w}; \mathbf{v})| &\leq \left(\frac{\rho}{\tau} + \rho \|\nabla \mathbf{u}_{meas}^k\|_{\infty} \right) \|\mathbf{w}\|_{L_2(\Omega_h)} \|\mathbf{v}\|_{L_2(\Omega_h)} \\
&\quad + \rho \|\mathbf{u}_{meas}^k + \mathbf{w}^{k-1}\|_{\infty} \|\mathbf{w}\|_{L_2(\Omega_h)} \|\nabla \mathbf{v}\|_{L_2(\Omega_h)} \\
&\quad + \mu \|\nabla \mathbf{w}\|_{L_2} \|\nabla \mathbf{v}\|_{L_2} + \|\nabla p\|_{L_2(\Omega_h)} \|\mathbf{v}\|_{L_2(\Omega_h)} + \|\nabla q\|_{L_2(\Omega_h)} \|\mathbf{w}\|_{L_2(\Omega_h)} \\
&\leq \left(\frac{\rho}{\tau\beta} + \frac{\rho}{\beta} \|\nabla \mathbf{u}_{meas}^k\|_{\infty} + \frac{\rho}{\beta} \|\mathbf{u}_{meas}^k + \mathbf{w}^{k-1}\|_{\infty} + \frac{\mu}{\beta} \right) \|(\mathbf{w}, p)\|_W \|(\mathbf{v}, q)\|_W \\
&\quad + \frac{1}{\sqrt{\beta}} \|\nabla p\|_{L_2(\Omega_h)} \|(\mathbf{v}, q)\|_W + \frac{1}{\sqrt{\beta}} \|\nabla q\|_{L_2(\Omega_h)} \|(\mathbf{w}, p)\|_W
\end{aligned}$$

And to end the proof we need to bound the pressure gradient:

$$\begin{aligned}
\|\nabla p\|_{L_2(\Omega_h)} &\leq \|\rho((\mathbf{u}_{meas}^k + \mathbf{w}^{k-1}) \cdot \nabla) \mathbf{w} + \rho(\mathbf{w} \cdot \nabla) \mathbf{u}_{meas}^k + \nabla p\|_{L_2(\Omega_h)} \\
&\quad + \|\rho((\mathbf{u}_{meas}^k + \mathbf{w}^{k-1}) \cdot \nabla) \mathbf{w} + \rho(\mathbf{w} \cdot \nabla) \mathbf{u}_{meas}^k\|_{L_2(\Omega_h)} \\
&\leq \sqrt{\frac{\mu}{\delta h^2}} \|(\mathbf{w}, p)\|_W + \|\rho(\mathbf{u}_{meas}^k + \mathbf{w}^{k-1})\|_{L_2(\Omega_h)} \|\nabla \mathbf{w}\|_{L_2(\Omega_h)} + \|\rho \nabla \mathbf{u}_{meas}^k\|_{L_2(\Omega_h)} \|\mathbf{w}\|_{L_2(\Omega_h)} \\
&\leq \left(\sqrt{\frac{\mu}{\delta h^2}} + \frac{1}{\sqrt{\beta}} \|\rho(\mathbf{u}_{meas}^k + \mathbf{w}^{k-1})\|_{L_2(\Omega_h)} + \frac{1}{\sqrt{\beta}} \|\rho \nabla \mathbf{u}_{meas}^k\|_{L_2(\Omega_h)} \right) \|(\mathbf{w}, p)\|_W
\end{aligned}$$

■

Lemma 5 *There exists a constant $C > 0$ such that:*

$$|\mathcal{L}_j(\mathbf{v}, q)| \leq C \|(\mathbf{v}, q)\|_W$$

Proof We proceed using Cauchy-Schwarz inequality and adding the reminder terms to obtain the W -norm:

$$\begin{aligned}
\|\mathcal{L}_j(\mathbf{v}, q)\| &\leq \frac{\rho}{\tau} \|\mathbf{w}^{k-1}\|_{L_2(\Omega_h)} \|\mathbf{v}\|_{L_2(\Omega_h)} + |\ell_j(\mathbf{v}, q)| \\
&\leq \frac{\rho}{\tau \sqrt{\beta}} \|\mathbf{w}^{k-1}\|_{L_2(\Omega_h)} \|(\mathbf{v}, q)\|_W + |\ell_j(\mathbf{v}, q)|
\end{aligned}$$

The last term can be bounded as:

$$\begin{aligned}
|\ell_j(\mathbf{v}, q)| &\leq \|\mathbf{f}^k\|_{L_2(\Omega_h)} \|\mathbf{v}\|_{L_2(\Omega_h)} + \mu \|\nabla \mathbf{u}_{meas}^k\|_{L_2(\Omega_h)} \|\mathbf{v}\|_{L_2(\Omega_h)} \\
&\quad + \sqrt{\delta \frac{h^2}{\mu}} \|\mathbf{f}^k\|_{L_2(\Omega_h)} \sqrt{\delta \frac{h^2}{\mu}} \left\| \left(\rho((\mathbf{u}_{meas}^k + \mathbf{w}^{k-1}) \cdot \nabla) \mathbf{v} + \rho(\mathbf{v} \cdot \nabla) \mathbf{u}_{meas}^k + \nabla q \right) \right\|_{L_2(\Omega_h)} \\
&\leq \left(\frac{1}{\beta} \|\mathbf{f}^k\|_{L_2(\Omega_h)} + \frac{\mu}{\beta} \|\nabla \mathbf{u}_{meas}^k\|_{L_2(\Omega_h)} + \sqrt{\delta \frac{h^2}{\mu}} \|\mathbf{f}^k\|_{L_2(\Omega_h)} \right) \|(\mathbf{v}, q)\|_W
\end{aligned}$$

■

Theorem 1 *There exists a unique solution in W of Problem (7) under condition (13) for all $k > 0$.*

Proof Since $\mathbf{w}^0 = \mathbf{0} \in [H^1(\Omega)]^3$, the bilinear and linear forms fulfill the requirements of the Lax-Milgram Theorem (i.e. Lemmas 3–5) for $k \geq 1$. ■

2.4 Time stability of the discrete solution

We can furthermore prove the following energy balance:

Theorem 2 For (\mathbf{w}^k, p^k) solution of Problem (7), with $\ell_j(\mathbf{v}, q) = 0$ it holds

$$\|\mathbf{w}^k\|_{L_2(\Omega)}^2 \leq \|\mathbf{w}^{k-1}\|_{L_2(\Omega)}^2 \quad (14)$$

under the condition

$$\mu \geq C_\Omega^2 3\rho \|\nabla \mathbf{u}_{meas}^k\|_\infty \quad (15)$$

Proof Testing (7) with $\mathbf{v} = \mathbf{w}^k$ and $q = p^k$ and using similar arguments as in Lemma 3, it is obtained

$$\begin{aligned} \frac{\rho}{2\tau} \|\mathbf{w}^k\|_{L_2(\Omega_h)}^2 - \frac{\rho}{2\tau} \|\mathbf{w}^{k-1}\|_{L_2(\Omega_h)}^2 &= -\mu \|\nabla \mathbf{w}^k\|_{L_2(\Omega_h)}^2 - \int_\Omega \left(\rho(\mathbf{w}^k \cdot \nabla) \mathbf{u}_{meas}^k \right) \cdot \mathbf{w}^k \\ &\quad - \frac{\rho}{2\tau} \|\mathbf{w}^k - \mathbf{w}^{k-1}\|_{L_2(\Omega_h)}^2 - S_k^{press}(\mathbf{w}^k, p^k; \mathbf{w}^k, p^k) \end{aligned}$$

where the two first terms in the right-hand-side come from the continuous problem, and the two last terms are dissipative due to the numerical scheme. Bounding the former using Poincaré's inequality and the later by zero we obtain

$$\frac{\rho}{2\tau} \|\mathbf{w}^k\|_{L_2(\Omega_h)}^2 - \frac{\rho}{2\tau} \|\mathbf{w}^{k-1}\|_{L_2(\Omega_h)}^2 \leq (-\mu C_\Omega^{-2} + 3\rho \|\nabla \mathbf{u}_{meas}^k\|_\infty) \|\mathbf{w}^k\|_{L_2(\Omega_h)}^2$$

what combined with condition (15) leads to relation (14) ■

3 Numerical experiments using synthetic data

3.1 General procedure

All testcases were created in the following way:

- A reference flow \mathbf{v} is created using a finite element solver setup, that will be detailed later for each of the examples, on an unstructured mesh with a fine time step.
- In order to simulate a realistic imaging setup, a box mesh with the desired image resolution is created around the computational mesh where the reference simulation was performed. The velocity field from the reference simulation was interpolated to that box mesh, such that $\mathbf{v}_H = \mathcal{I}_H(\mathbf{v})$, with \mathcal{I}_H an usual piecewise linear Lagrangian interpolation.
- Then, the degrees-of-freedom of \mathbf{v}_H are arranged as multidimensional array, which will serve to create the images. One array is created for each of the three velocity components, denoted by $\mathcal{V}_1, \mathcal{V}_2, \mathcal{V}_3$.
- Phase-contrast MRI (PC-MRI) acquisitions were simulated from the velocity data for each array \mathcal{V}_j . For 4D flow, four magnetization complex arrays are usually measured: three flow-sensitive magnetization arrays $\mathcal{M}_j = m_0 \exp(i\phi_0 + i\pi\mathcal{V}_j/venc)$, $i = 1, 2, 3$, and a flow-compensated magnetization, $\mathcal{M}_0 = m_0 \exp(i\phi_0)$, which does not depend

on the velocity. In all these experiments, the value of ϕ_0 is assumed constant in space and time and equal to $7.5 \cdot 10^{-2} \text{ rad}$, and m_0 assumed constant and equal to 0.5 on the non-zero velocity voxels and also constant and equal to 0.1 for the rest. The $venc$ parameter is a predefined velocity which enforces all the velocities being in the interval $(-venc, venc)$ [18]. The resulting velocity-to-noise ratio (VNR) is then proportional to the $venc$, therefore the $venc$ should be chosen as small as possible, what commonly leads to velocity wraps in 4D flow images.

- In order to study the performance of the method in realistic MRI applications, we perturbed the magnetizations and consequently the reconstructed velocity adding noise and aliasing (varying the $venc$):
 - Additive gaussian noise was added into \mathcal{K}_j , $j = 0, \dots, 3$, being \mathcal{K}_j the discrete Fourier transform (DFT) of \mathcal{M}_j , which is in fact the quantity measured by the scanner.
 - Aliasing was explored setting the $venc$ parameter lower than the maximum true velocity. Therefore, when the velocity exceeds the $venc$ (in absolute value), the reconstructed velocity will be wrapped.
- The perturbed velocity is recovered by:

$$\tilde{\mathcal{V}}_j = \frac{venc}{\pi} \text{atan}(\tilde{\mathcal{M}}_j / \tilde{\mathcal{M}}_0)$$

with $/$ representing an element-wise division of the arrays and $\tilde{\mathcal{M}}_j$ corresponding to the magnetization reconstructed using the perturbed measurements of \mathcal{K}_j .

- An image mask is created from the reference simulation on the box mesh. Then, a new semi-structured tetrahedral mesh following the aortic shape is created using the algorithm reported in [17]. The velocity is then defined as a \mathbb{P}_1 finite element field on such mesh in order to visualize the results and to quantify the errors to the reference solution, which is also interpolated to the semi-structured mesh.
- The aforementioned procedure is repeat for every dataset. Problem (7) was solved using such interpolated, perturbed velocity in the right-hand-side as \mathbf{u}_{meas}^k , with $j = 0, \dots, N$. For the pressure stabilization term a $\delta = 10^{-4}$ parameter was used. For visualization of every step see Figure 1.

3.2 Synthetic Womersley flow

We consider a Womersley flow in a cylinder of length $H = 5 \text{ cm}$ and radius $R = 1 \text{ cm}$, driven by an oscillatory pressure drop of amplitude $\delta p = 2000 \text{ barye}$ and frequency $\omega = 1 \text{ Hz}$. The physical parameters of the fluid were: density $\rho = 1.0 \text{ gr/cm}^3$ and dynamic viscosity $\mu = 0.035 \text{ P}$, resulting in a Womersley number of $\alpha = R\sqrt{\omega\rho/\mu} = 13.3$. The solution was

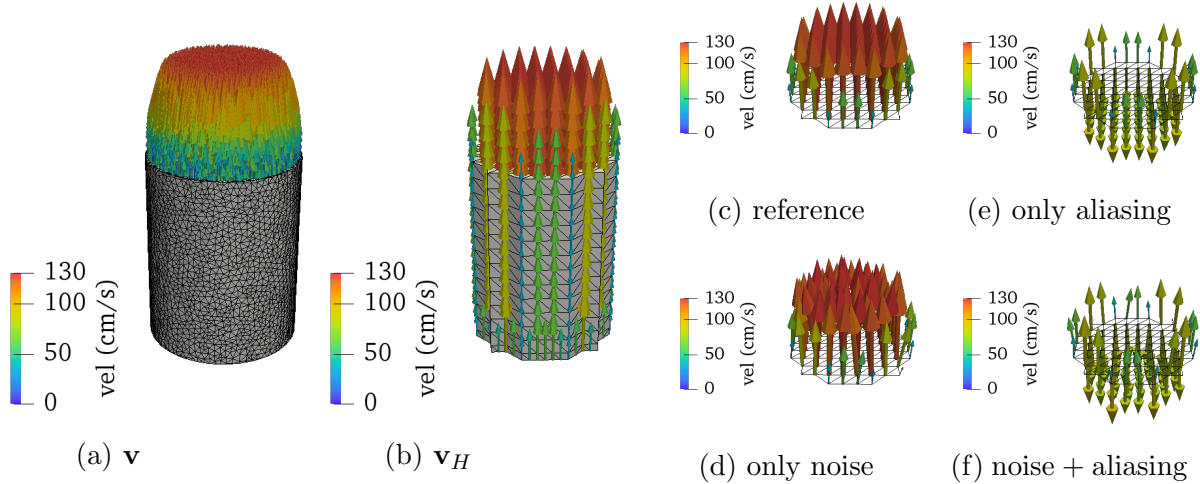


Figure 1: Generation of measurements for the Womersley test case. a) Velocity profile in the unstructured mesh. b) Resulting velocity after interpolation into the mask, together with the generated mesh. c)-f) Profiles of the perturbed velocity: c) reference, d) only aliasing, e) only noise and f) noise and aliasing.

obtained solving a Stokes problem with a backwards Euler scheme in the time derivative, using a monolithic P1/P1 finite element method implemented in FEniCS [19]. A PSPG stabilization term was added with a parameter $\delta = 10^{-4}$. For boundary condition, a non-slip condition for the velocity was used at the walls, with a Dirichlet condition at the inlet for the pressure. The mesh was built with unstructured elements consisting of 229,379 tetrahedrons and 39,556 vertices. Finally, the total simulation time was $T_f = 1$ s with a timestep of $dt = 0.01$ s. From this reference simulation, the velocity measurements were perturbed following the procedure detailed in Section 3.1 using a measurement mask with voxel size of $2 \times 2 \times 2$ mm³ and measurement time step of 0.03 s. A gaussian noise was added into the k-space resulting in a noise in the velocity with variance 2.87% of the maximum velocity. Two venvs were chosen in order to be the 120% and 80% of the maximum velocity, resulting in the values of 204 and 136 cm/s respectively. The resulting measurement are shown in Figure 1.

Figure 2 shows the corrector \mathbf{w} at the time of peak velocity together with the measurements \mathbf{u}_{meas} for the four measurements sets. Furthermore, L^2 -norm per mesh element of $\nabla \cdot \mathbf{u}_{meas}$ is shown for comparison. As expected, in the case without noise, the divergence field shows no sensitivity to aliasing (since the aliased Womersley flow also has zero divergence), while \mathbf{w} , and in particularly the longitudinal component is clearly perturbed by aliasing. For the noisy cases, the values of \mathbf{w} are further perturbed, while the behavior with/without aliasing was hold. Moreover, the difference field $\delta \mathbf{u} = \mathbf{u}_{true} - \mathbf{u}_{meas}$ is shown for comparison with the corrector. In this way, a perfect corrected case will be when $\delta \mathbf{u} = \mathbf{w}$. From the figures, in both aliased cases \mathbf{w} shows a major difference respect to $\delta \mathbf{u}$, being the discontinuity due to aliasing unfeasible to reconstruct by the method, as expected since $\mathbf{w} \in [H^1(\Omega)]^3$.

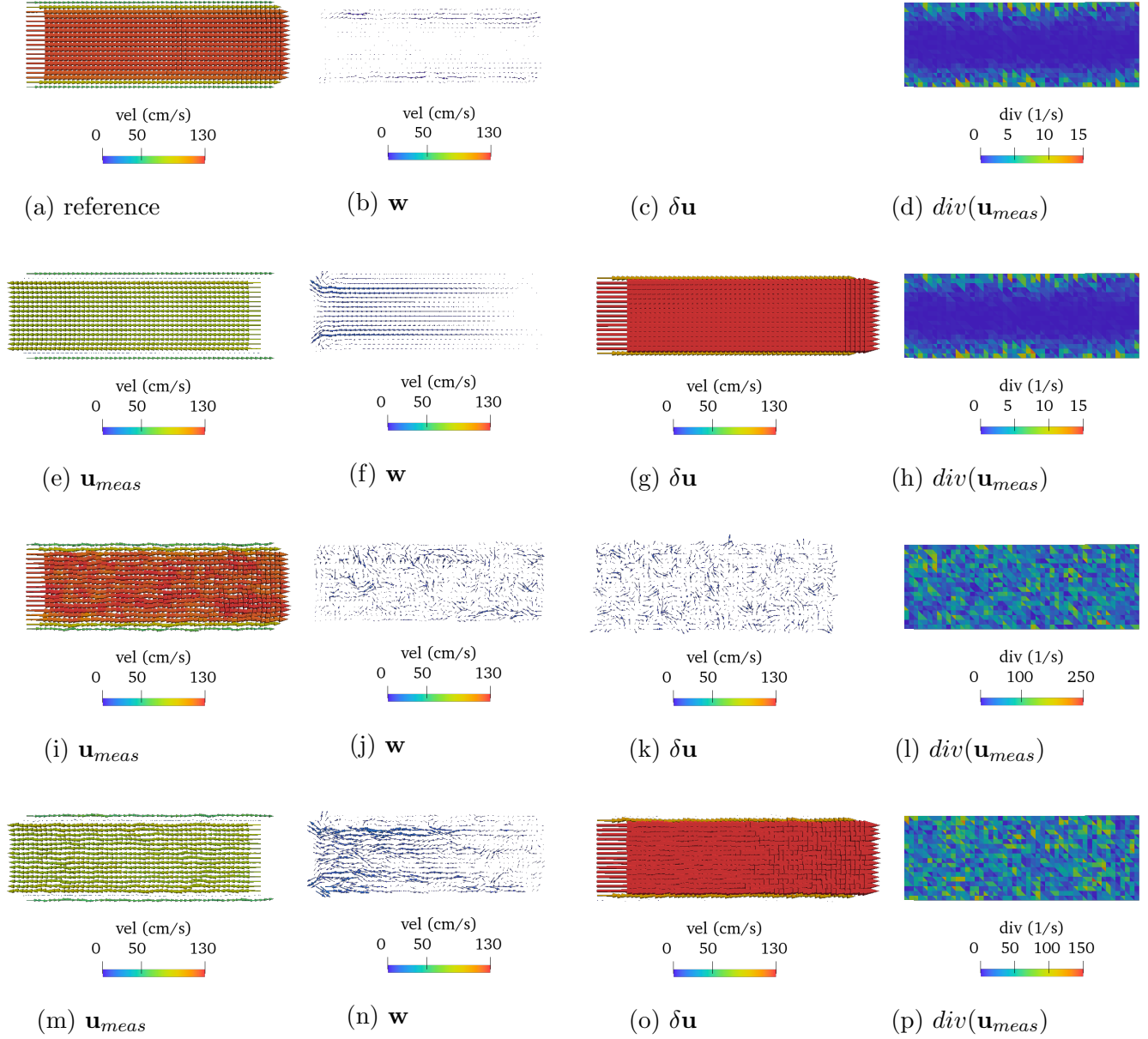


Figure 2: Fields for the Womersley flow. Figures are as follows with its case: (a)-(d) non-perturbed, (e)-(h) only aliasing, (i)-(l) only noise and (m)-(p) noise and aliasing.

Nevertheless, in the aliasing free case \mathbf{w} and $\delta\mathbf{u}$ are substantially closer.

Figure 3 presents the time evolution of the $L^2(\Omega_h)$ -norms of the same quantities. The norms of the corrector components were normalized by the $venc$ in order to be dimensionless and by the square root of the domain’s volume. The divergence of the measurements was arbitrary rescaled for visualizing it together with the other curves. For the reference case, $\delta\mathbf{u}$ is zero by definition while \mathbf{w} is not. This comes from the fact that reference and corrector computations are performed with different numerical schemes (mesh and discretization).

In the case of a pure noise perturbation, the transversal components of \mathbf{w} are smaller than the corresponding ones of $\delta\mathbf{u}$. In contrast, the z -component increases over time. This occurs probably because, since the corrector does not exactly compensate for the errors in the data in a certain time step due to the restriction in the function space, this induces a larger error in the next time steps.

The latter seems however not to be the case for aliased measurements. In that scenario, all components of \mathbf{w} jump at the moment that aliasing appears, being the one aligned with the (aliased) flow, considerably more sensitive. In contrast, the divergence is less sensitive to aliasing, only when noise is present this seems to contribute to its detection. Note also that \mathbf{w} needs some time to decrease after aliasing disappears from the data due to the “memory” induced by the time derivative.

3.3 Synthetic aortic flow

In order to test the corrector under a more complex scenario, synthetic data was generated in a drawn-aortic mesh with a mild coartation in the descending aorta and consist of 2,752,064 tetrahedrons and 510,755 vertices. An incompressible Navier-Stokes problem was solved with a monolithic formulation with Temam and PSPG stabilizations. For the PSPG term, a $\delta = 10^{-2}$ parameter was used. Additionally, blackflow stabilization was added in every outlet of the system. The boundary conditions were set as: (1) A Dirichlet condition at the inflow Γ_{inlet} , (2) Non-slip condition at the walls Γ_{wall} and (3) a three-element Windkessel (R_p, C, R_d) condition for the rest of the outlets $\Gamma_{w,i}$. In this way, $\partial\Omega = \Gamma_{inlet} \cup \Gamma_{wall} \cup_{j=1}^4 \Gamma_{w,i}$. The constants were tuned by hand in order to have a standard physiological flow regime. For the numerical values of these boundary parameters see Table 1. The simulation was performed with a total time of $T_f = 0.8$ s with a timestep of $dt = 0.001$ s. The physical properties of the fluid were: density $\rho = 1.119$ gr/cm³ and dynamic viscosity $\mu = 0.035$ P. Afterwards, and identical procedure as in the previous section was applied to the resulting measurements, adding a gaussian noise in the k-space resulting in a noise in the velocity with a variance of 3.8% of the maximum velocity. Moreover two $vencs$ as the 120% and 70% of the maximum velocity were chosen, resulting in the values of 194 and 113 cm/s respectively. The velocity field and its interpolation are shown in Figure 4.

Results for the corrector method applied to the perturbed measurements are shown in Figure 5. For the non-perturbed case, the corrector grows in zones with high velocities. As before, for the pure noise case, the corrector shows better agrees with $\delta\mathbf{u}$. High values at the walls cannot be reproduced because of the chosen homogeneous Dirichlet condition.

In the pure aliased case, the corrector field grows when the aliasing occurs, but not

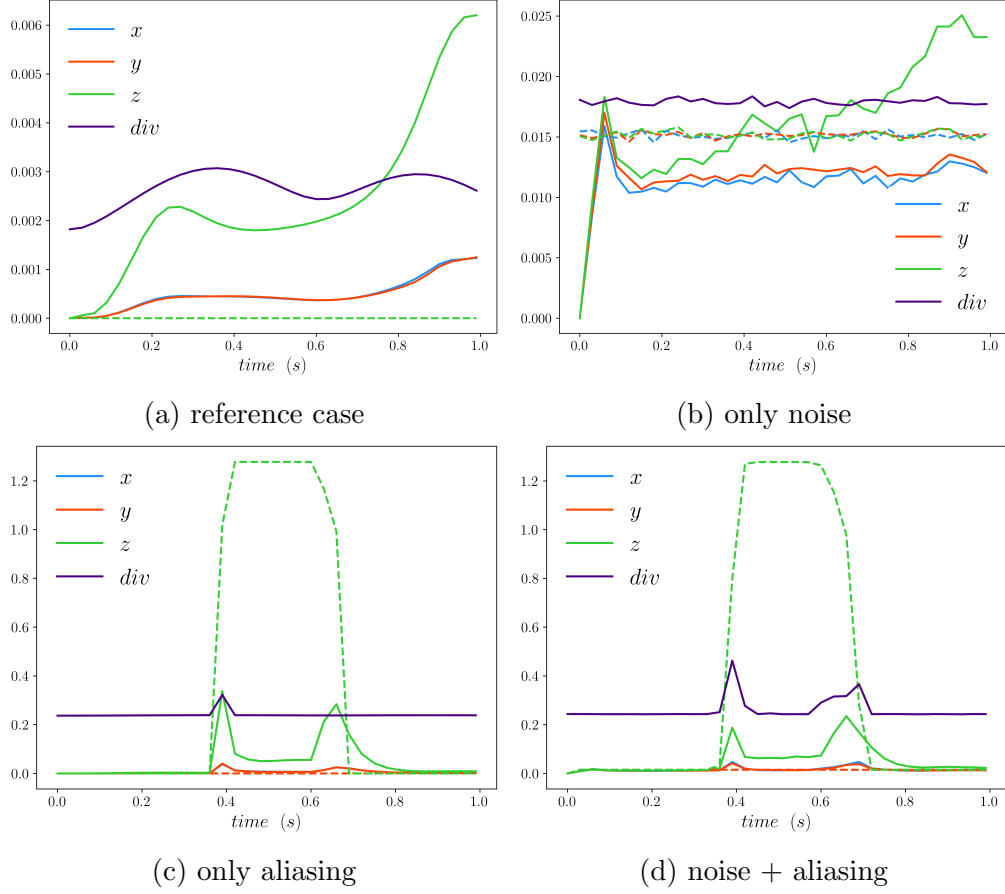


Figure 3: Normalized $L^2(\Omega_h)$ norms of the components of \mathbf{w} (continuous line), $\delta\mathbf{u}$ (dashed lines), and divergence of the measurements over time.

	$\Gamma_{w,1}$	$\Gamma_{w,2}$	$\Gamma_{w,3}$	$\Gamma_{w,4}$
R_p ($\text{dyn} \cdot \text{s} \cdot \text{cm}^{-5}$)	250	250	250	10
R_d ($\text{dyn} \cdot \text{s} \cdot \text{cm}^{-5}$)	$1 \cdot 10^{-4}$	$1 \cdot 10^{-4}$	$1 \cdot 10^{-4}$	$1 \cdot 10^{-2}$
C ($\text{dyn}^{-1} \cdot \text{cm}^5$)	$8 \cdot 10^3$	$8 \cdot 10^3$	$8 \cdot 10^3$	$1 \cdot 10^3$

Table 1: Numerical values of the three-element Windkessel parameters for every outlet.

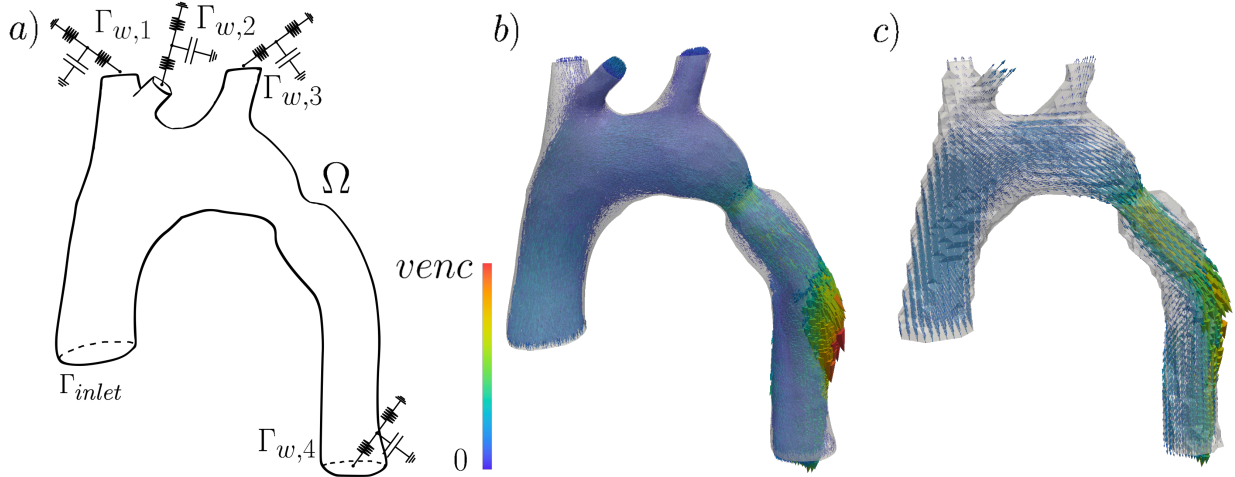


Figure 4: (a) Boundary conditions in the drawn aorta. (b) Velocity field in the reference mesh at the peak systole. (c) Interpolated velocity in the voxel-type mesh

as much as $\delta \mathbf{u}$ as it was the case in the Womersley flow example. Also, now a coupling among the components of the corrector field appears. For the case with noise and aliasing, a combination of the two behaviors is evident. In contrast, the divergence field shows only little sensitivity to aliasing and exhibit a overall increase in the presence of noise.

4 Numerical examples using real 4D flow MRI data

4.1 Experimental phantom

A realistic thoracic aortic phantom was scanned using a clinical 1.5 T MR scanner (Philips Achieva, Best, The Netherlands) with a four-element phased-array body coil. The phantom was made of flexible silicone and a 11 mm orifice coartation made of Technyl was placed in the descending aorta (for further details of the setup and the phantom see [20, 21]). A blood mimicking fluid made with 60 % water and 40 % glycerol (Orica Chemicals, Watkins, CO) was used in the system. The fluid results in a density of 1.119 g/cm^3 , dynamic viscosity of 0.0483 P and T1 value of 900 ms , which are typical parameters for human blood. The acquisition was performed with a v_{enc} of 350 cm/s and using a cartesian sampling sequence with no k-space undersampling involved. In MRI, the noise level of the image increases when decreasing the spatial resolution and other artifacts appear close to the boundaries known as *partial volume effect*. Therefore, three isotropic voxel sizes (coarse: 2.5 mm , mid: 2.0 mm and 1.5 mm) were acquired in order to investigate the results of the corrector field.

Figure 6 shows the 4D flow measurements with their corrector field \mathbf{w} at the moment of peak systole. First, as expected \mathbf{w} increases with more artifacts coming from the reduced voxel size. Also the corrected velocity, i.e. $\mathbf{u}_{meas} + \mathbf{w}$, was added in order to see the impact of the corrector field for every scenario. High spurious velocity voxels near the boundary are

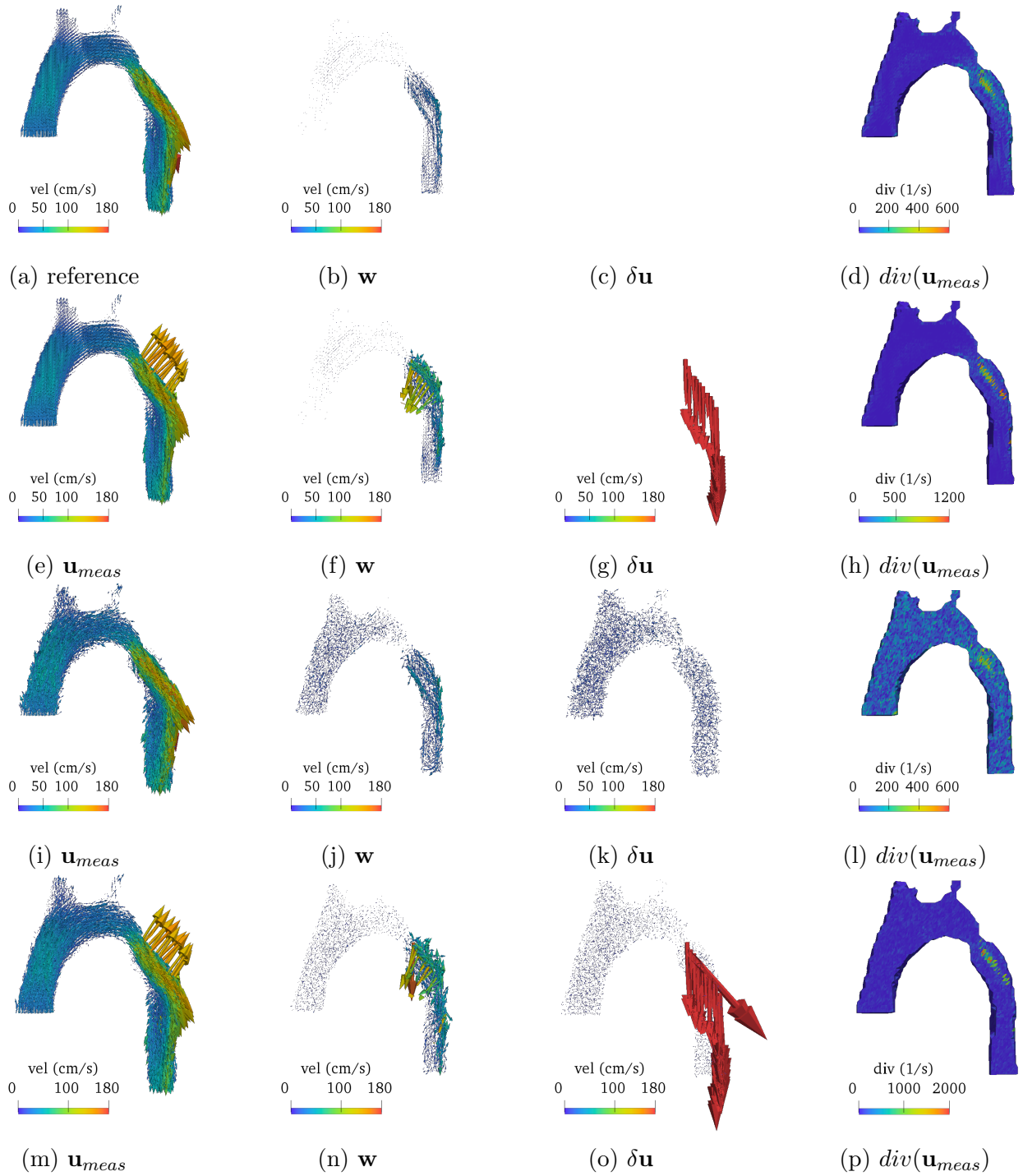


Figure 5: Fields for the aortic flow. Figures are as follows with its case: (a)-(d) non-perturbed, (e)-(h) only aliasing, (i)-(l) only noise and (m)-(p) noise and aliasing.

mostly due partial volume effects. Due to the homogeneous Dirichlet boundary condition's choice at the walls, \mathbf{w} cannot correct these voxels since it vanishes at the boundary.

Note also that for all three resolutions the corrector tends to grow in zones with high velocities, as in the jets in the ascending and descending aorta, and in zones with turbulent flow, e.g behind the jet in the ascending aorta. Therefore, the addition of the corrector into the measurements shows an smoother effect at the turbulent part in the ascending aorta at the coarctation.

5 Conclusion

We presented a new mathematical model – including its discretization – with the potential of quantifying the deviation of the data from a perfect physical velocity. The model is derived from the consistency of the data with the Navier-Stokes equations. The vectorial nature of the estimator has been shown potential in the detectability of artifacts and in the denoising of the measurements in a postprocessing step.

Synthetic data experiments show advantages of the field in the detectability on typical artifacts affecting 4D flow MRI such as noise and aliasing. The main advantage of this quality estimator is its vectorial nature, opening the space to a more detailed analysis than a scalar field such as the divergence of the measurements. With real 4D flow MRI, we showed how the corrector value increases when decreasing data quality. In this scenario, this method offers a way to reduce the noise level adding the corrective field as a postprocessing filter.

The method also indicates zones where the data could be misrepresenting the blood flow, which is valuable information specially when further flow quantification needs to be processed. These zones are in this work, where turbulence could be present in the blood flow, being the results in agreement with others studies that have shown limitations on the 4D flow acquisition on those regimes.

Still, we evidence some limitations of the current approach which may be subject of future works. For instance, the corrector field can not completely capture strong discontinuities in the measurements, i.e. in aliasing-contaminated measurements, mainly due to the regularity of the solution imposed by the solution spaces required in the model. Nevertheless, for noise-contaminated measurements, the corrector could be used for reducing the noise, which was confirmed in the real data. This could be the first application of this new model in a clinical environment.

Acknowledgements

This project has received funding from the European Research Council (ERC) under the European Union's Horizon 2020 research and innovation programme (grant agreement No 852544 - CardioZoom).

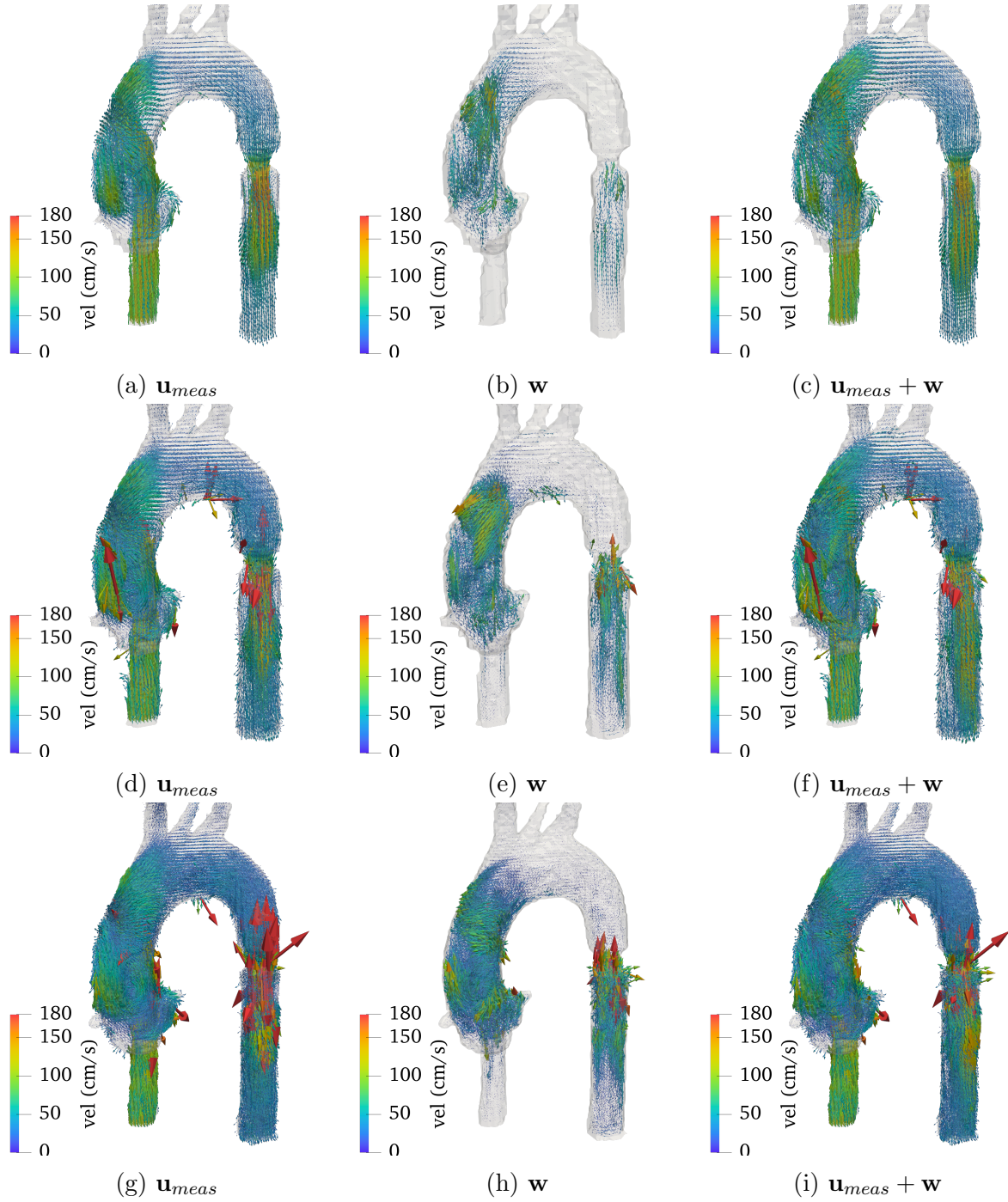


Figure 6: Measurements, corrector fields and corrected velocities for all the cases. The resolutions are as follows: (a)-(c) *coarse*, (d)-(f) *mid* and (g)-(i) *fine*.

Appendix A

In this part we want give a brief but concluding compared analysis of both formulations for $\nabla \cdot \mathbf{w}$, namely *model A*:

$$\nabla \cdot \mathbf{w}_A = 0, \quad (16)$$

which is the one used throughout the manuscript and *model B*, coming from solving Equation (7) but with an additional right-hand-side for the divergence coming from the constraint $\nabla \cdot \mathbf{u} = 0$, i.e.:

$$\nabla \cdot \mathbf{w}_B = -\nabla \cdot \mathbf{u}_{meas} + \frac{1}{|\Omega|} \int_{\partial\Omega} \mathbf{u}_{meas} \cdot \mathbf{n}. \quad (17)$$

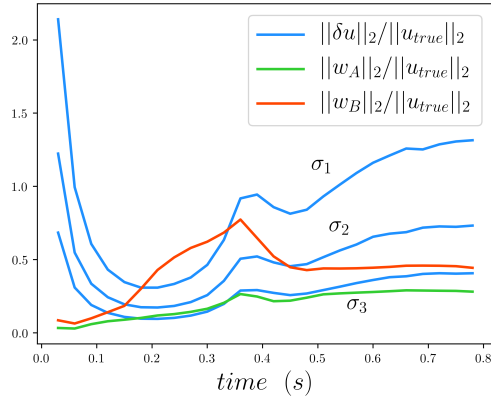
Note that as it was explained in Remark 2, the linear momentum conservation used in *model A* already contains the assumption that $\nabla \cdot \mathbf{u} = 0$.

In order to assess both models, we compute a corrector field using an aortic flow simulated data as measurements (for details see Section 3.3) without any noise, only reinterpolating the reference simulation onto the box mesh. The resulting corrector fields were compared against $\delta \mathbf{u} = \mathbf{u} - \mathbf{u}_{meas}$, with \mathbf{u}_{meas} generated from three noise levels in the k-space $\sigma_1, \sigma_2, \sigma_3$, leading to standard deviations in the velocity data of 2.2, 3.9, 6.9% of the maximum absolute value of the velocity, respectively.

Figure 7a shows the evolution of normalized $L_2(\Omega)$ norms for the noise level as well as the corrector fields for both divergence models. All the noise levels start from a high level value since at the beginning of the cardiac cycle, the noise is large in comparison to the true velocity. It can also be seen that the corrector using *model B* is about 4 times larger than with model A used in the rest of the manuscript. The corrector with *model B* is then of the order of measurements error with 6.9% of standard deviation. Figures 7b-7e show the perturbed measurements for every noise level. Figures 7f and 7g present the corrector fields obtained using the reference solution for *model A* and *model B*, respectively. Both models appear to be significantly different in particular near the coarctation, being *model A* substantially smaller than *model B* and in particular *model B* developing a sort of jet of magnitude close to the actual reference velocity field. Also in the regions more far from the coarctation, the corrector with model *model B* also has larger values than with *model A*.

References

- [1] Michael Markl, Alex Frydrychowicz, Sebastian Kozerke, Mike Hope, and Oliver Wieben. 4d flow mri. *Journal of Magnetic Resonance Imaging*, 36(5):1015–1036, 2012.
- [2] Gilles Soulat, Patrick McCarthy, and Michael Markl. 4d flow with mri. *Annual Review of Biomedical Engineering*, 22, 2020.
- [3] K.P. Pruessmann, M. Weiger, M.B. Scheidegger, and P. Boesiger. Sense: Sensitivity encoding for fast mri. *Magn Reson Med.*, 42(5):952–962, 1999.



(a) $L_2(\Omega)$ -norms evolution for the corrector fields for noise-free measurements and true error for different noise levels in the measurements.

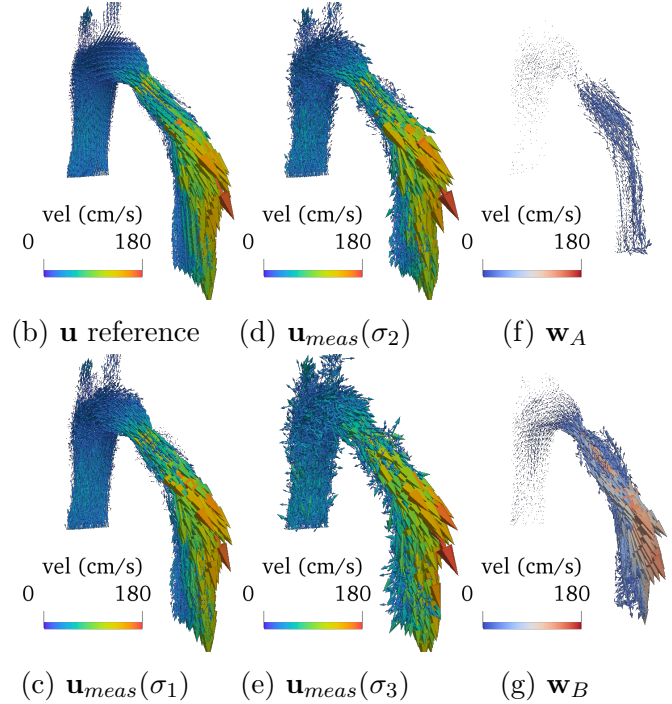


Figure 7: Comparison between the divergence constraint models for the corrector.

- [4] M.A. Griswold, P.M Jakob, R.M Heidenmann, M Nittka, V. Jellus, J. Wang, B. Kiefer, and A. Haase. Generalized autocalibrating partially parallel acquisitions (grappa). *Magn Reson Med.*, 47(9):1202–1210, 2002.
- [5] S. Kozerke, J. Tsao, R. Razavi, and P. Boesiger. Accelerating cardiac cine 3d imaging using k-t blast. *Magn Reson Med.*, 52:19–26, 2004.
- [6] Christof Baltes, Sebastian Kozerke, Michael S Hansen, Klaas P Pruessmann, Jeffrey Tsao, and Peter Boesiger. Accelerating cine phase-contrast flow measurements using k-t blast and k-t sense. *Magnetic resonance in medicine*, 54(6):1430–1438, 2005.
- [7] Urs Gamper, Peter Boesiger, and Sebastian Kozerke. Compressed sensing in dynamic mri. *Magnetic Resonance in Medicine: An Official Journal of the International Society for Magnetic Resonance in Medicine*, 59(2):365–373, 2008.
- [8] Liliana E Ma, Michael Markl, Kelvin Chow, Hyungkyu Huh, Christoph Forman, Alireza Vali, Andreas Greiser, James Carr, Susanne Schnell, Alex J Barker, et al. Aortic 4d flow mri in 2 minutes using compressed sensing, respiratory controlled adaptive k-space reordering, and inline reconstruction. *Magnetic resonance in medicine*, 81(6):3675–3690, 2019.
- [9] Taha Sabri Koltukluoglu, Sven Hirsch, Christian Binter, Sebastian Kozerke, Gábor Székely, and Aymen Laadhari. A robust comparison approach of velocity data between

- mri and cfd based on divergence-free space projection. In *2015 IEEE 12th International Symposium on Biomedical Imaging (ISBI)*, pages 1393–1397. IEEE, 2015.
- [10] Thekla H Oechtering, Malte M Sieren, Peter Hunold, Anja Hennemuth, Markus Huellebrand, Michael Scharfschwerdt, Doreen Richardt, Hans-Hinrich Sievers, Jörg Barkhausen, and Alex Frydrychowicz. Time-resolved 3-dimensional magnetic resonance phase contrast imaging (4d flow mri) reveals altered blood flow patterns in the ascending aorta of patients with valve-sparing aortic root replacement. *The Journal of thoracic and cardiovascular surgery*, 159(3):798–810, 2020.
- [11] Joaquin Mura, A Matias Pino, Julio Sotelo, Israel Valverde, Cristian Tejos, Marcelo E Andia, Pablo Irarrazaval, and Sergio Uribe. Enhancing the velocity data from 4d flow mr images by reducing its divergence. *IEEE transactions on medical imaging*, 35(10):2353–2364, 2016.
- [12] Julia Busch, Daniel Giese, Lukas Wissmann, and Sebastian Kozerke. Reconstruction of divergence-free velocity fields from cine 3d phase-contrast flow measurements. *Magnetic resonance in medicine*, 69(1):200–210, 2013.
- [13] Frank Ong, Martin Uecker, Umar Tariq, Albert Hsiao, Marcus T Alley, Shreyas S Vasanawala, and Michael Lustig. Robust 4d flow denoising using divergence-free wavelet transform. *Magnetic resonance in medicine*, 73(2):828–842, 2015.
- [14] Claudio Santelli, Michael Loecher, Julia Busch, Oliver Wieben, Tobias Schaeffter, and Sebastian Kozerke. Accelerating 4d flow mri by exploiting vector field divergence regularization. *Magnetic resonance in medicine*, 75(1):115–125, 2016.
- [15] Emrah Bostan, Orestis Vardoulis, Davide Piccini, Pouya Dehghani Tafti, Nikolaos Stergiopoulos, and Michael Unser. Spatio-temporal regularization of flow-fields. In *2013 IEEE 10th International Symposium on Biomedical Imaging*, pages 836–839. IEEE, 2013.
- [16] H Švihlová, J Hron, J Málek, KR Rajagopal, and K Rajagopal. Determination of pressure data from velocity data with a view toward its application in cardiovascular mechanics. Part 1. Theoretical considerations. *International Journal of Engineering Science*, 2016, In press.
- [17] David Nolte, Jesús Urbina, Julio Sotelo, Leo Sok, Cristian Montalba, Israel Valverde, Axel Osses, Sergio Uribe, and Cristobal Bertoglio. Validation of 4D flow based relative pressure maps in the aorta. working paper or preprint, July 2020.
- [18] Hugo Carrillo, Axel Osses, Sergio Uribe, and Cristóbal Bertoglio. Optimal dual-vec unwrapping in phase-contrast mri. *IEEE transactions on medical imaging*, 38(5):1263–1270, 2018.
- [19] Anders Logg, Kent-Andre Mardal, Garth N. Wells, et al. *Automated Solution of Differential Equations by the Finite Element Method*. Springer, 2012.

- [20] Jesús Urbina, Julio A Sotelo, Daniel Springmüller, Cristian Montalba, Karis Letelier, Cristián Tejos, Pablo Irrarázaval, Marcelo E Andia, Reza Razavi, Israel Valverde, et al. Realistic aortic phantom to study hemodynamics using mri and cardiac catheterization in normal and aortic coarctation conditions. *Journal of Magnetic Resonance Imaging*, 44(3):683–697, 2016.
- [21] Cristian Montalba, Jesus Urbina, Julio Sotelo, Marcelo E Andia, Cristian Tejos, Pablo Irrarazaval, Daniel E Hurtado, Israel Valverde, and Sergio Uribe. Variability of 4d flow parameters when subjected to changes in mri acquisition parameters using a realistic thoracic aortic phantom. *Magnetic resonance in medicine*, 79(4):1882–1892, 2018.

Centro de Investigación en Ingeniería Matemática (CI²MA)

PRE-PUBLICACIONES 2020 - 2021

- 2020-20 NICOLAS BARNAFI, GABRIEL N. GATICA, DANIEL E. HURTADO, WILLIAN MIRANDA, RICARDO RUIZ-BAIER: *New primal and dual-mixed finite element methods for stable image registration with singular regularization*
- 2020-21 GONZALO A. BENAVIDES, SERGIO CAUCAO, GABRIEL N. GATICA, ALEJANDRO A. HOPPER: *A new non-augmented and momentum-conserving fully-mixed finite element method for a coupled flow-transport problem*
- 2020-22 RAIMUND BÜRGER, ELVIS GAVILÁN, DANIEL INZUNZA, PEP MULET, LUIS M. VILLADA: *Exploring a convection-diffusion-reaction model of the propagation of forest fires: computation of risk maps for heterogeneous environments*
- 2020-23 GABRIEL N. GATICA, RICARDO OYARZÚA, RICARDO RUIZ-BAIER, YURI D. SOBRAL: *Banach spaces-based analysis of a fully-mixed finite element method for the steady-state model of fluidized beds*
- 2020-24 JESSIKA CAMAÑO, SERGIO CAUCAO, RICARDO OYARZÚA, SEGUNDO VILLA-FUENTES: *A posteriori error analysis of a momentum conservative Banach-spaces based mixed-FEM for the Navier-Stokes problem*
- 2020-25 RAIMUND BÜRGER, JULIO CAREAGA, STEFAN DIEHL: *A method-of-lines formulation for a model of reactive settling in tanks with varying cross-sectional area*
- 2020-26 RAIMUND BÜRGER, CHRISTOPHE CHALONS, RAFAEL ORDOÑEZ, LUIS M. VILLADA: *A multiclass Lighthill-Whitham-Richards traffic model with a discontinuous velocity function*
- 2020-27 TOMÁS BARRIOS, EDWIN BEHRENS, ROMMEL BUSTINZA: *An a posteriori error estimate for a dual mixed method applied to Stokes system with non null source terms*
- 2020-28 RODOLFO ARAYA, CRISTIAN CÁRCAMO, ABNER POZA: *An adaptive stabilized finite element method for the Darcy's equations with pressure dependent viscosities*
- 2020-29 SERGIO CAUCAO, RICARDO OYARZÚA, SEGUNDO VILLA-FUENTES: *A posteriori error analysis of a momentum and thermal energy conservative mixed-FEM for the Boussinesq equations*
- 2020-30 REINALDO CAMPOS-VARGAS, CLAUDIA FUENTEALBA, IGNACIA HERNÁNDEZ, MARTEN HERTOG, CLAUDIO MENESES, DIEGO PAREDES, ROMINA PEDRESCHI, VIRGILIO UARROTA: *Can metabolites at harvest be used as physiological markers for modelling the softening behaviour of Chilean "Hass" avocados destined to local and distant markets?*
- 2021-01 CRISTÓBAL BERTOGGIO, CRISTIAN CÁRCAMO, JEREMÍAS GARAY, HERNÁN MELLA, JOAQUÍN MURA, JULIO SOTELO, SERGIO URIBE: *A new mathematical model for verifying the Navier-Stokes compatibility of 4D flow MRI data*

Para obtener copias de las Pre-Publicaciones, escribir o llamar a: DIRECTOR, CENTRO DE INVESTIGACIÓN EN INGENIERÍA MATEMÁTICA, UNIVERSIDAD DE CONCEPCIÓN, CASILLA 160-C, CONCEPCIÓN, CHILE, TEL.: 41-2661324, o bien, visitar la página web del centro: <http://www.ci2ma.udec.cl>



**CENTRO DE INVESTIGACIÓN EN
INGENIERÍA MATEMÁTICA (CI²MA)
Universidad de Concepción**



Casilla 160-C, Concepción, Chile
Tel.: 56-41-2661324/2661554/2661316
<http://www.ci2ma.udec.cl>

